Use of a Single ^{11}C-*Meta*-Hydroxyephedrine Scan for Assessing Flow–Innervation Mismatches in Patients with Ischemic Cardiomyopathy

Hendrik J. Harms[1], Mark Lubberink[2], Stefan de Haan[3], Paul Knaapen[3], Marc C. Huisman[1], Robert C. Schuit[1], Albert D. Windhorst[1], Cornelis P. Allaart[3], and Adriaan A. Lammertsma[1]

[1]*Department of Radiology and Nuclear Medicine, VU University Medical Center, Amsterdam, Netherlands;* [2]*Department of Nuclear Medicine and PET Research, Uppsala University, Uppsala, Sweden; and* [3]*Department of Cardiology, VU University Medical Center, Amsterdam, Netherlands*

Mismatch between areas of reduced myocardial blood flow (MBF) and reduced myocardial innervation (defect areas) may be used to estimate the risk for ventricular arrhythmias. The presence of a mismatch zone can be derived using a combined protocol consisting of both an MBF scan and an ^{11}C-*meta*-hydroxyephedrine (^{11}C-HED) scan. The rate of influx from blood to myocardium (K_1) of ^{11}C-HED is proportional to MBF and can potentially be used as an index for defining MBF defects. The aim of this study was to assess whether K_1 derived from an ^{11}C-HED scan can be used as an index of MBF, potentially allowing for an assessment of MBF–innervation mismatch areas from a single ^{11}C-HED scan. **Methods:** Seventeen patients with known ischemic cardiomyopathy underwent dynamic ^{15}O-water and ^{11}C-HED scans. Discrete arterial blood samples were taken during ^{11}C-HED scans for metabolite correction of the image-derived input function. ^{11}C-HED influx rate was obtained using a single-tissue-compartment model and compared with transmural MBF (MBF_T), defined as MBF as measured with ^{15}O-water multiplied by perfusable tissue fraction. Defect sizes were obtained from parametric K_1 and MBF_T images, using 50% of a remote control segment as the cutoff value. **Results:** There was a significant correlation between MBF_T and K_1 ($y = 0.40x + 0.05$ mL·g^{-1}·min^{-1}, $r = 0.80$, $P < 0.001$), although K_1 was significantly lower than MBF_T (slope of the regression line significantly different from 1, $P < 0.001$). Correlation between MBF_T and K_1 defect sizes was high ($y = 0.89x + 1.38\%$, $r = 0.95$, $P < 0.001$), with no significant difference in mean defect size based on K_1 or MBF_T (20.9% ± 11.3% and 20.1% ± 10.7% for MBF_T and K_1, respectively, $P = 0.41$). **Conclusion:** ^{11}C-HED influx rate K_1 can be used as an alternative to a separate MBF scan for assessing mismatch areas between MBF and myocardial innervation.

Key Words: innervation–blood flow mismatch; sympathetic denervation; ^{11}C-HED; arrhythmias

J Nucl Med 2015; 56:1706–1711
DOI: 10.2967/jnumed.115.154377

There has been long-standing interest in noninvasive imaging of myocardial sympathetic innervation for the prediction of life-threatening ventricular arrhythmias or implantable cardioverter defibrillator discharges using PET (*1–5*) or SPECT (*6–8*). It has been shown (*9–11*) that, in myocardial infarction, the area of reduced innervation often exceeds the area of reduced myocardial blood flow (MBF) (*9–14*). Furthermore, in a porcine model of myocardial infarction, it has been shown that the occurrence of such MBF–innervation mismatch zones is related to inducible ventricular tachycardias originating from these zones (*15*). The potential of MBF–innervation mismatch zones in risk assessment has been demonstrated in the recent PAREPET study (*16*), in which patients developing sudden cardiac arrest had a significantly larger area of viable but denervated myocardium. Therefore, noninvasive imaging for identifying MBF–innervation mismatch zones may play a role in risk stratification of patients with ischemic cardiomyopathy who are considered for cardioverter defibrillator implantation.

MBF–innervation mismatch zones are generally quantified using separate MBF and innervation scans. The use of separate scans, however, has some disadvantages: motion artifacts between scans may occur, overall study duration is prolonged, and radiation dose to the patient is increased. Clearly, a single-scan protocol for defining MBF–innervation mismatches would be preferable.

Recently, it has been shown that the kinetics of ^{11}C-*meta*-hydroxyephedrine (^{11}C-HED) can be described reliably using a single-tissue-compartment model with corrections for left and right ventricular spill-over (*17*). The underlying tracer kinetic model has two parameters: K_1 and k_2, which represent the rate of ^{11}C-HED transfer from blood to myocardium (influx rate) and the rate of transfer from myocardium to blood (clearance rate), respectively. The volume of distribution of ^{11}C-HED, defined as the ratio of K_1 to k_2, represents net uptake, that is, equilibrium distribution between tissue and plasma, and can be used as a measure of innervation.

K_1 is dependent on both the extraction fraction of ^{11}C-HED and MBF. Therefore, if the extraction fraction of ^{11}C-HED is constant across a clinically relevant range of resting MBF levels, changes in ^{11}C-HED K_1 would reflect changes in MBF. In this case a single ^{11}C-HED scan could be used to define MBF–innervation mismatch areas.

Therefore, the aim of this study was to assess whether K_1 derived from an ^{11}C-HED scan can be used as an index of MBF.

MATERIALS AND METHODS

Patient Population

Seventeen patients (mean age, 67 y; range, 43–80 y; 13 men) with ischemic cardiomyopathy and a left ventricular ejection fraction below 35% based on cardiac MR imaging were included. Ischemic

Received Jan. 13, 2015; revision accepted Jul. 16, 2015.
For correspondence or reprints contact: Hendrik J. Harms, Department of Nuclear Medicine and PET Research, VU University Medical Center, P.O. Box 7057, 1007 MB Amsterdam, The Netherlands.
E-mail: h.harms@vumc.nl
Published online Jul. 30, 2015.

cardiomyopathy was defined as the presence of one or more stenoses of greater than 50% as determined from a coronary angiogram and delayed contrast enhancement on cardiac MR imaging. The study was approved by the Medical Ethics Review Committee of the VU University Medical Center, and all participants gave written informed consent before inclusion.

Scanning Protocol

The patients underwent a dynamic ^{15}O-water scan, followed by an ^{11}C-HED scan in the same session. All studies were performed on a Gemini TF-64 (Philips Healthcare) PET/CT scanner (*18*).

A 5-mL bolus injection of 370 MBq of ^{15}O-water (0.8 mL·s^{-1}), followed by 35 mL of saline (2 mL·s^{-1}), was administered simultaneously with the start of a list-mode emission scan of 6 min. The injected dose was chosen to remain within the linear range of the scanner, the upper limit of which is at a singles counting rate of about 35 Mcps (*19*). Maximum singles counting rates in the present study were approximately 32 Mcps during the first pass of the bolus. This PET scan was followed immediately by a respiration-averaged low-dose CT scan (55 mAs; rotation time, 1.5 s; pitch, 0.825; collimation, 64 × 0.625; acquiring 20 cm in 11 s) during normal breathing. The emission scan was reconstructed into 22 frames (1 × 10, 8 × 5, 4 × 10, 2 × 15, 3 × 20, 2 × 30, and 2 × 60 s) using the 3-dimensional row action maximum-likelihood algorithm and applying all appropriate corrections for scanner normalization, dead time, decay, randoms, scatter, and attenuation, with the attenuation correction being based on the corresponding low-dose CT scan. Frames consisted of 45 planes of 144 × 144 voxels with voxels having dimensions of 4 × 4 × 4 mm. The effective radiation dose for a ^{15}O-water study and low-dose CT was estimated as 1.5 mSv.

^{11}C-HED was synthesized as described previously (*17*). At least 10 min after the end of the ^{15}O-water scan, 370 MBq of ^{11}C-HED were injected as a 5-mL bolus (0.8 mL·s^{-1}) followed by a 35-mL saline flush (2 mL·s^{-1}), simultaneously starting a 60-min list-mode emission scan. After the emission scan, a slow low-dose CT scan was performed to correct for attenuation, similar to the ^{15}O-water scan. Images were reconstructed into 36 frames (1 × 10, 8 × 5, 4 × 10, 3 × 20, 5 × 30, 5 × 60, 4 × 150, 4 × 300, and 2 × 600 s) using the 3-dimensional row action maximum-likelihood algorithm and applying all appropriate corrections. The effective radiation dose for a ^{11}C-HED study and low-dose CT was estimated as 2.5 mSv.

Blood Sampling

Before the scanning session, all patients received an indwelling radial artery cannula for withdrawal of discrete blood samples during the dynamic ^{11}C-HED scan. A total of 7 arterial samples of 7 mL each were collected at 2.5, 5, 10, 20, 30, 40, and 60 min after ^{11}C-HED injection. Blood samples were analyzed for blood and plasma activity concentrations and for radiolabeled plasma metabolites of ^{11}C-HED as previously described (*17*).

Input Functions

Input functions were obtained using in-house–developed software, *Cardiac VUer* (*20,21*). For both ^{15}O-water and ^{11}C-HED, 1-cm-diameter regions of interest were placed over the ascending aorta in at least 5 transaxial image planes in the frame showing the first pass of the injected bolus. These regions of interest were combined into one volume of interest for the ascending aorta. A second set of regions of interest was placed over the right ventricular cavity in 5 transaxial planes, with the region-of-interest boundaries at least 1 cm from the right ventricular wall to avoid spill-over of myocardial activity. Again, these regions of interest were combined into one right ventricular volume of interest. Both volumes of interest were then transferred to the full dynamic images to obtain arterial whole-blood and right ventricular time–activity curves.

Next, for ^{11}C-HED only, plasma–to–whole-blood ratios derived from the manual blood samples were fitted to a sigmoid function. Parent fractions derived from these manual samples were fitted to a sigmoid function. Finally, the parent plasma curve was obtained by multiplying the arterial whole-blood curve by the fitted plasma–to–whole-blood ratio and parent fraction curves.

Segmental Analysis

Sixteen myocardial segments, excluding the most distal apical segment, were drawn manually on short-axis images according to the 17-segment model of the American Heart Association (*22*), using software developed in-house within Matlab 7 (The MathWorks). For ^{11}C-HED, segments were defined on the final frame of the dynamic images, whereas for ^{15}O-water, parametric images of perfusable tissue fraction (PTF) were used. The obtained segment templates were projected onto all frames of their corresponding short-axis dynamic emission scans to extract segmental time–activity curves. These were fitted to a single-tissue-compartment model for both ^{15}O-water and ^{11}C-HED using standard nonlinear least-squares regression according to Equations 1 and 2 for ^{15}O-water (*23*) and ^{11}C-HED (*17*), respectively:

$$C_{PET}(t) = PTF \times MBF \cdot C_A(t) \otimes e^{-\frac{MBF}{V_T} \cdot t} + V_A \times C_A(t) + V_{RV} \times C_{RV}(t) \quad \text{Eq. 1}$$

$$C_{PET}(t) = K_1 \cdot C_P(t) \otimes e^{-k_2 \cdot t} + V_A \times C_A(t) + V_{RV} \times C_{RV}(t), \quad \text{Eq. 2}$$

in which $C_{PET}(t)$, $C_A(t)$, $C_{RV}(t)$, and $C_P(t)$ represent radioactivity concentrations in tissue, whole blood, right ventricular blood, and parent tracer in plasma, respectively. V_A represents left ventricular spill-over and V_{RV} right ventricular spill-over. For ^{15}O-water, total distribution volume V_T was fixed to 0.91 mL·g^{-1} (*24*), whereas for ^{11}C-HED, V_T was calculated as K_1/k_2.

K_1 represents the average ^{11}C-HED influx rate in both perfusable and nonperfusable tissue. However, MBF as measured with ^{15}O-water represents MBF in perfusable tissue alone (*25*), and the fraction of perfusable tissue is reflected in PTF. To make an appropriate comparison between ^{11}C-HED K_1 and MBF as measured with water, MBF was multiplied by PTF to obtain MBF in perfusable and nonperfusable tissue, or transmural MBF (MBF_T).

Parametric Images

For ^{15}O-water, parametric images were generated using a basis function implementation (*20,26,27*) of the single-tissue-compartment model (Eq. 1) with corrections for blood volume, spill-over (*23*), and PTF (*28*). One hundred basis functions were used with exponentially spaced values of MBF/V_T between 0.1 and 2.5 min^{-1}. For ^{11}C-HED, a basis function implementation of Equation 2 was used, applying 100 basis functions with exponentially spaced values of k_2 between 0.002 and 0.1 min^{-1} and corrections for left and right ventricular spill-over. For ^{11}C-HED, parametric images of V_T were obtained by dividing parametric images of K_1 by parametric images of k_2.

For both ^{11}C-HED and ^{15}O-water, parametric images of anatomic tissue fraction were generated according to Equation 3:

$$\text{Anatomic tissue fraction} = 1.06 \cdot (CT_{norm} - V_A - V_{RV}), \quad \text{Eq. 3}$$

in which CT_{norm} represents the normalized low-dose CT scan and 1.06 represents the density of blood. In voxels with $V_A + V_{RV} > 0.75$, V_A or $V_{RV} > 0.60$, or anatomic tissue fraction < 0.25, MBF, K_1, and V_T were set to zero to avoid spurious noise–induced high values outside the heart or in blood vessels as described previously (*20,29*). Finally, MBF_T images were obtained by multiplying MBF images by PTF images.

Data Analysis

Correlation between MBF_T and K_1 was assessed using linear regression. For each patient, 4 adjacent segments were selected and used as a control region. These segments did not border infarct segments and showed normal innervation (V_T). If scar and denervation sizes were too large to identify 4 such segments, at least 2 adjacent segments were used instead. For both MBF_T and K_1, defect size was defined as the percentage of pixels below a percentage (between 20% and 80%, in increments of 5%) of the average of the control region. Similarly, parametric V_T images were obtained and used to define innervation defects using the same control region. MBF–innervation mismatch sizes were obtained by subtracting the K_1 or MBF_T defect size from the V_T defect size. To avoid differences in volume-of-interest definition between ^{11}C-HED and ^{15}O-water scans, defect sizes were assessed for the entire left ventricle rather than for each segment individually. Correlation and agreement between defect sizes were assessed using linear regression, Bland–Altman analysis, and paired *t* tests using Matlab 7. Finally, the Dice similarity coefficient (DSC) was calculated for the polar maps to quantify agreement in both defect location and size.

RESULTS

The scans of 2 patients had visually identifiable motion and were excluded from further analysis. For the remaining 15 patients, the correlation between absolute MBF_T and K_1 is presented in Figure 1. There was a significant correlation between MBF_T and K_1 ($y = 0.40x + 0.05$ mL·g^{-1}·min^{-1}, $r = 0.80$, $P < 0.001$), indicating that the extraction fraction of ^{11}C-HED is relatively constant across the range of MBF_T values encountered. The slope of the regression line was significantly lower than 1 ($P = 0.02$), and the intercept was significantly different from 0 ($P < 0.001$).

For all relative cutoff values, Table 1 shows the correlations, slopes and intercepts of the regression lines, *P* values of paired *t* tests, and average DSC. For cutoffs between 30% and 70%, an excellent correlation ($r \geq 0.90$) was found and slopes of the regression lines were not significantly different from unity, except for the 35% cutoff value. DSC was above 0.80 for all except an 80% cutoff.

Typical examples of parametric MBF_T and K_1 images are presented in Figure 2, showing reduced MBF_T and K_1 in the territory of the left anterior descending artery. Corresponding polar plots are shown in Figure 3. The correlation between defect sizes was high ($y = 0.89x + 1.38\%$, $r = 0.95$, $P < 0.001$), as shown in Figure 4 using a 50% cutoff. The slope of the regression line was not significantly different from 1 ($P = 0.24$), and the intercept of the regression line was not significantly different from 0 ($P = 0.50$). A paired *t* test showed that defect sizes based on K_1 were not significantly different from those based on MBF_T ($P = 0.41$). In addition, when the regression line was forced through the origin, the slope was 0.95, which was not significantly different from 1 ($P = 0.20$). DSC (0.88 ± 0.05; range, 0.77–0.96) showed good agreement between MBF_T and K_1 at the polar map level, indicating that defect locations were similar. Figure 5 shows the correlation between mismatch sizes derived using MBF_T and K_1. A high correlation between mismatch sizes was found ($y = 0.89x + 2.2\%$, $r = 0.92$, $P < 0.001$), with slope and intercept not being significantly different from 1 ($P = 0.32$) and 0 ($P = 0.21$), respectively. In addition, paired *t* testing showed that mismatch sizes were not significantly smaller for K_1 than for MBF_T (20.9% ± 11.3% and 20.1% ± 10.7% for MBFT and K_1, respectively, $P = 0.41$).

DISCUSSION

In the present proof-of-concept study, a method to assess MBF–innervation mismatch size from a single ^{11}C-HED scan was studied, using the influx rate K_1 of ^{11}C-HED to obtain an index of MBF rather than measuring MBF separately using an additional

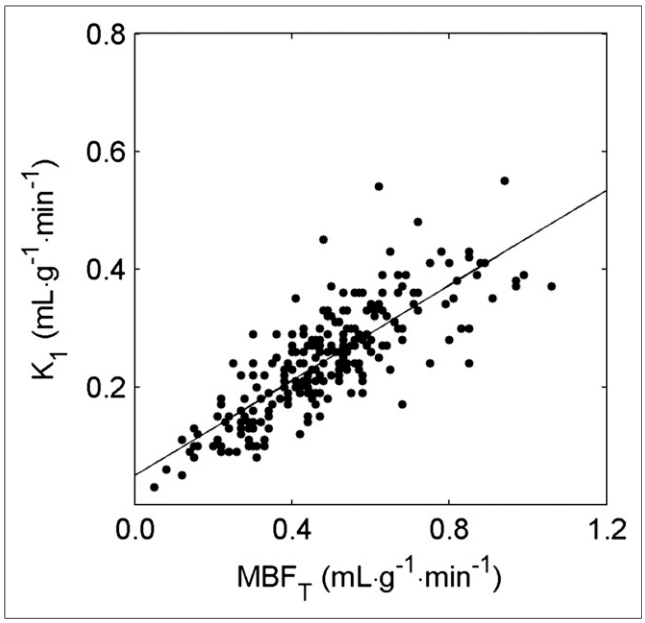

FIGURE 1. Correlation between K_1 of ^{11}C-HED and absolute MBF_T on heart segment level. This correlation was significant ($r = 0.80$, $P < 0.001$). Slope of regression line was 0.40, which was significantly lower than 1 ($P < 0.001$). Intercept was 0.05, which was significantly different from 0 ($P < 0.001$).

TABLE 1
Comparison of Defect Sizes Based on ^{11}C-HED Influx Rate K_1 and MBF_T as Measured with ^{15}O-Water

Relative cutoff	*r*	Slope	Intercept	Slope no intercept	*P* (*t* test)	DSC
20%	0.82	0.66*	0.67	0.74*	0.34	0.95
25%	0.86	0.72*	0.81	0.80*	0.30	0.94
30%	0.94	0.83	0.80	0.89	0.44	0.93
35%	0.97	0.86	0.83	0.91*	0.29	0.92
40%	0.97	0.89	0.90	0.94	0.37	0.91
45%	0.97	0.89	1.34	0.95	0.50	0.89
50%	0.95	0.89	1.46	0.95	0.41	0.88
55%	0.94	0.88	2.04	0.95	0.36	0.86
60%	0.93	0.85	3.11	0.94	0.33	0.85
65%	0.91	0.84	4.29	0.95	0.40	0.83
70%	0.90	0.83	5.95	0.97	0.74	0.82
75%	0.87	0.82	7.92	0.99	0.98	0.80
80%	0.85	0.80	9.99	1.00	0.83	0.79

*Significant deviation from 1 ($P < 0.05$).

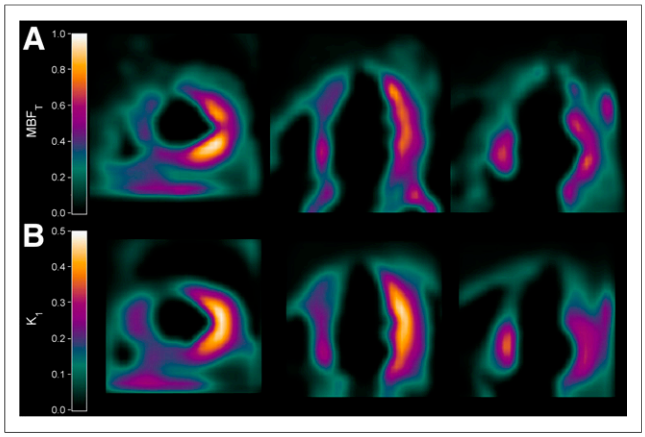

FIGURE 2. Typical example of parametric images of MBF_T (top) and K_1 (bottom) of patient with myocardial infarct in anterior, septal, and apical walls.

^{15}O-water scan. Shortening the scanning protocol reduces the risk of motion and total radiation burden. In addition, patient throughput is increased while the method still provides accurate data on mismatch areas.

Direct comparison between K_1 and MBF_T showed that K_1 significantly underestimated MBF_T, suggesting that the extraction of ^{11}C-HED is about 40%–50%. However, relative cutoff values compared with remote control segments (*15,16*) were used to define defect areas, and a consistent underestimation of K_1 as compared with MBF_T was expected to play a limited role in definition of defect areas. This was indeed confirmed in our study as illustrated by the excellent correlation between defect sizes obtained with K_1 and MBF_T. In addition, the slope of the regression line was not significantly different from 1, Bland–Altman analysis showed no significant differences between the two defect sizes, and paired *t* tests showed no significant differences, indicating the potential of using K_1 instead of MBF_T for mismatch assessment. However, the limited extraction of ^{11}C-HED rules out use of ^{11}C-HED as a tracer of absolute MBF.

This study focused on the use of 50% of a healthy reference region as a cutoff value for both MBF_T and K_1. Because the optimal method for defining patient-specific cutoff values is as yet unknown, a value of 50% may not be optimal. Therefore, this study included relative cutoff values between 20% and 80% of the value of a healthy reference region (Table 1). For 20%–25% and for 75%–80%, correlation was reduced to an *r* value of below 0.90, and for cutoffs of 20%–25% and 35%, the slopes of the regression lines started to deviate significantly from unity. However, for the range of 30%–60%, both correlation coefficients and slopes were comparable with the results obtained when a 50% cutoff value was used. In addition, paired *t* tests showed no significant difference for any of the assessed cutoff values. This indicates that defect areas for K_1 and MBF_T are similar for a wide range of relative cutoff values for differentiating between healthy and defect tissue. In addition, for different cutoff values, average DSC for all patients was slightly lower at increased cutoffs. However, average DSC was above 0.80 for all cutoff values studied, except for 80%. The optimal cutoff value or a method to define defect areas for both blood flow and innervation has to be defined in larger clinical studies with long-term follow-up. This method might also be different when using relative uptake images (*15,16*) or fully quantitative parameters, and more clinical studies are warranted.

In this study, ^{11}C-HED K_1 was compared with the product of MBF and PTF because MBF derived from a ^{15}O-water scan represents MBF in perfusable tissue whereas ^{11}C-HED K_1 represents the transmural rate of influx, that is, in both perfusable and nonperfusable tissue within a region. Assuming no influx of ^{11}C-HED in nonperfusable tissue, uptake signal is reduced in direct proportion to the fraction of nonperfusable tissue. However, MBF derived from ^{15}O-water is calculated using washout rates, and since nonperfusable tissue has no uptake of ^{15}O-water, it does not contribute to the observed washout rate of ^{15}O-water. This results in differences between MBF and ^{11}C-HED influx rate K_1 in regions with both perfusable and nonperfusable tissue. Since the fraction of perfusable tissue is routinely calculated as PTF, the product of

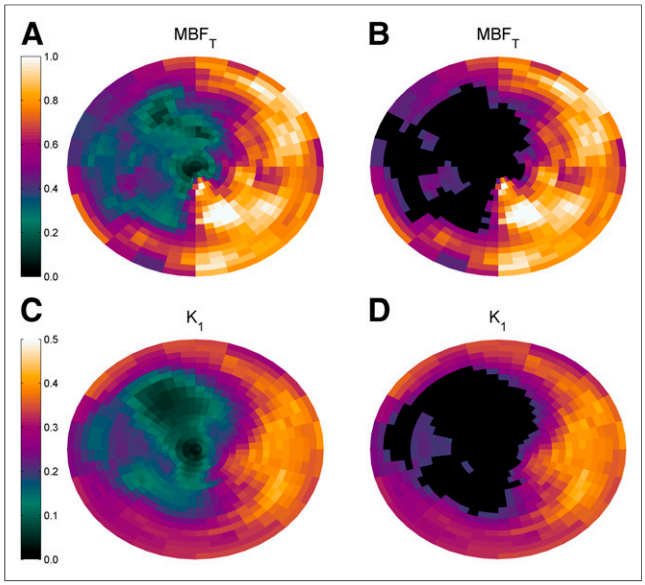

FIGURE 3. Polar maps of MBF_T and K_1 of same patient as in Figure 2. Total defect size, indicated by black areas in B and D, was 28.7% based on MBF_T and 27.0% based on K_1. DSC was 0.87.

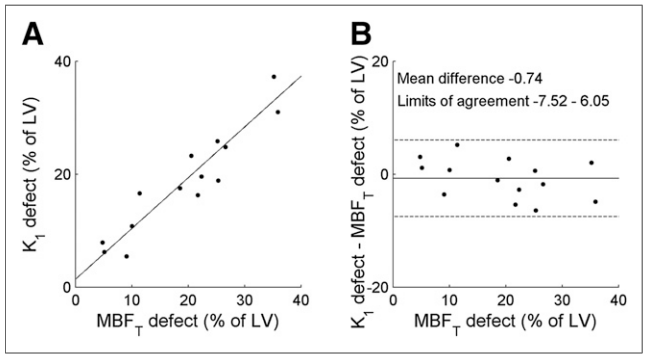

FIGURE 4. Correlation (left) and Bland–Altman (right) plots of defect size based on MBF_T and K_1. Slope of regression line was 0.89, which was not significantly different from 1 (P = 0.24). Intercept was 1.38, which was not significantly different from 0 (P = 0.50). No significant correlation was found on Bland–Altman analysis (P = 0.21). LV = left ventricle.

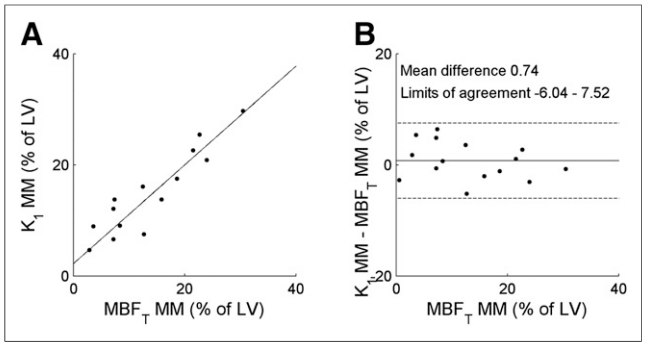

FIGURE 5. Correlation (left) and Bland–Altman plot (right) of mismatch size based on MBF_T and K_1. Slope of regression line was 0.89, which was not significantly different from 1 ($P = 0.32$). Intercept of regression line was 2.20, which was not significantly different from 0 ($P = 0.21$). No significant correlation was found on Bland–Altman analysis ($P = 0.29$). LV = left ventricle; MM = mismatch.

MBF and PTF should resemble total (transmural) MBF in these regions. It is therefore appropriate to compare ^{11}C-HED K_1 with MBF_T.

The results of this study are in contrast to those of Rimoldi et al. (*30*), in which no correlation between MBF and ^{11}C-HED K_1 was found in dogs. There are, however, two major differences between the studies. First, in the present study, ^{11}C-HED K_1 was compared with the product of MBF and PTF, that is, transmural MBF, whereas Rimoldi et al. used regular MBF as obtained with ^{15}O-water. Comparing MBF with K_1 may be inappropriate and yield inaccurate results. To illustrate this, in the present study the correlation between regular nontransmural MBF and ^{11}C-HED K_1 was significantly lower, although still significant, with an r value of 0.67. Second, the range of MBF values in the present study was much larger than that of Rimoldi et al., as only patients with ischemic cardiomyopathy, and hence myocardial infarctions and large heterogeneities in MBF, were included. The dogs used by Rimoldi et al. showed regions of denervation but no infarctions, and therefore the range of MBF values was relatively small.

This study had several limitations. First, the number of subjects was relatively small ($n = 17$) and larger studies might be required before definitive omission of separate MBF scans can be advocated. In addition, the scans of 2 patients (12%) had to be excluded because of visually identifiable motion, and more subtle motion in the remaining patients cannot be excluded. Finally, a large-scale clinical validation is required before any conclusions regarding the application of mismatch zones from ^{11}C-HED alone can be drawn.

CONCLUSION

The rate of influx (K_1) of ^{11}C-HED can be used as a potential alternative to a separate MBF scan when assessing mismatch size between MBF and innervation in patients with ischemic cardiomyopathy. This alternative reduces scan duration, radiation dose, and risk of patient motion between scans, but the clinical utility of this mismatch size requires further clinical validation in larger patient cohorts before the method can be used.

DISCLOSURE

The costs of publication of this article were defrayed in part by the payment of page charges. Therefore, and solely to indicate this fact, this article is hereby marked "advertisement" in accordance with 18 USC section 1734. This work was supported financially by Philips Healthcare. No other potential conflict of interest relevant to this article was reported.

ACKNOWLEDGMENTS

We thank Amina Elouahmani, Femke Jongsma, Judith van Es, Nazerah Sais, Nghi Pham, Robin Hemminga, and Suzette van Balen for scanning of the patients; Henri Greuter, Kevin Takkenkamp, and Marissa Rongen for production of ^{15}O-water and blood analysis; and Martien Mooijer, Jonas Eriksson, Anneloes Rijnders, Rolf van Kooij, and Johan van den Hoek for synthesis of ^{11}C-HED.

REFERENCES

1. Chakraborty PK, Gildersleeve DL, Jewett DM, et al. High yield synthesis of high specific activity R-(−)-[^{11}C]epinephrine for routine PET studies in humans. *Nucl Med Biol.* 1993;20:939–944.
2. Goldstein DS, Chang PC, Eisenhofer G, et al. Positron emission tomographic imaging of cardiac sympathetic innervation and function. *Circulation.* 1990;81:1606–1621.
3. Münch G, Nguyen NT, Nekolla S, et al. Evaluation of sympathetic nerve terminals with [^{11}C]epinephrine and [^{11}C]hydroxyephedrine and positron emission tomography. *Circulation.* 2000;101:516–523.
4. Rosenspire KC, Haka MS, Van Dort ME, et al. Synthesis and preliminary evaluation of carbon-11-meta-hydroxyephedrine: a false transmitter agent for heart neuronal imaging. *J Nucl Med.* 1990;31:1328–1334.
5. Schwaiger M, Kalff V, Rosenspire K, et al. Noninvasive evaluation of sympathetic nervous system in human heart by positron emission tomography. *Circulation.* 1990;82:457–464.
6. Dae MW, O'Connell JW, Botvinick EH, et al. Scintigraphic assessment of regional cardiac adrenergic innervation. *Circulation.* 1989;79:634–644.
7. Kline RC, Swanson DP, Wieland DM, et al. Myocardial imaging in man with I-123 meta-iodobenzylguanidine. *J Nucl Med.* 1981;22:129–132.
8. Wieland DM, Wu J, Brown LE, Mangner TJ, Swanson DP, Beierwaltes WH. Radiolabeled adrenergic neuron-blocking agents: adrenomedullary imaging with [^{131}I]iodobenzylguanidine. *J Nucl Med.* 1980;21:349–353.
9. Jacobson AF, Senior R, Cerqueira MD, et al. Myocardial iodine-123 meta-iodobenzylguanidine imaging and cardiac events in heart failure: results of the prospective ADMIRE-HF (AdreView Myocardial Imaging for Risk Evaluation in Heart Failure) study. *J Am Coll Cardiol.* 2010;55:2212–2221.
10. Paul M, Schafers M, Kies P, et al. Impact of sympathetic innervation on recurrent life-threatening arrhythmias in the follow-up of patients with idiopathic ventricular fibrillation. *Eur J Nucl Med Mol Imaging.* 2006;33:866–870.
11. Yukinaka M, Nomura M, Ito S, Nakaya Y. Mismatch between myocardial accumulation of ^{123}I-MIBG and ^{99m}Tc-MIBI and late ventricular potentials in patients after myocardial infarction: association with the development of ventricular arrhythmias. *Am Heart J.* 1998;136:859–867.
12. Boogers MJ, Borleffs CJ, Henneman MM, et al. Cardiac sympathetic denervation assessed with 123-iodine metaiodobenzylguanidine imaging predicts ventricular arrhythmias in implantable cardioverter-defibrillator patients. *J Am Coll Cardiol.* 2010;55:2769–2777.
13. Inoue H, Zipes DP. Results of sympathetic denervation in the canine heart: supersensitivity that may be arrhythmogenic. *Circulation.* 1987;75:877–887.
14. Kammerling JJ, Green FJ, Watanabe AM, et al. Denervation supersensitivity of refractoriness in noninfarcted areas apical to transmural myocardial infarction. *Circulation.* 1987;76:383–393.
15. Sasano T, Abraham MR, Chang KC, et al. Abnormal sympathetic innervation of viable myocardium and the substrate of ventricular tachycardia after myocardial infarction. *J Am Coll Cardiol.* 2008;51:2266–2275.
16. Fallavollita JA, Heavey BM, Luisi AJ Jr, et al. Regional myocardial sympathetic denervation predicts the risk of sudden cardiac arrest in ischemic cardiomyopathy. *J Am Coll Cardiol.* 2014;63:141–149.
17. Harms HJ, de Haan S, Knaapen P, et al. Quantification of [^{11}C]-meta-hydroxyephedrine uptake in human myocardium. *EJNMMI Res.* 2014;4:52.
18. Surti S, Kuhn A, Werner ME, Perkins AE, Kolthammer J, Karp JS. Performance of Philips Gemini TF PET/CT scanner with special consideration for its time-of-flight imaging capabilities. *J Nucl Med.* 2007;48:471–480.

19. Lubberink M, van der Veldt A, Knaapen P, et al. Measurement of tumor and myocardial perfusion using ^{15}O-water and a clinical PET-CT scanner [abstract]. *J Nucl Med.* 2009;50(suppl 2):238.
20. Harms HJ, Knaapen P, de Haan S, Halbmeijer R, Lammertsma AA, Lubberink M. Automatic generation of absolute myocardial blood flow images using [^{15}O]H_2O and a clinical PET/CT scanner. *Eur J Nucl Med Mol Imaging.* 2011;38:930–939.
21. Harms HJ, Nesterov SV, Han C, et al. Comparison of clinical non-commercial tools for automated quantification of myocardial blood flow using oxygen-15-labelled water PET/CT. *Eur Heart J Cardiovasc Imaging.* 2014;15:431–441.
22. Cerqueira MD, Weissman NJ, Dilsizian V, et al. Standardized myocardial segmentation and nomenclature for tomographic imaging of the heart: a statement for healthcare professionals from the Cardiac Imaging Committee of the Council on Clinical Cardiology of the American Heart Association. *Circulation.* 2002;105:539–542.
23. Hermansen F, Rosen SD, Fath-Ordoubadi F, et al. Measurement of myocardial blood flow with oxygen-15 labelled water: comparison of different administration protocols. *Eur J Nucl Med.* 1998;25:751–759.
24. Bergmann SR, Herrero P, Markham J, Weinheimer CJ, Walsh MN. Noninvasive quantitation of myocardial blood flow in human subjects with oxygen-15-labeled water and positron emission tomography. *J Am Coll Cardiol.* 1989;14:639–652.
25. Yamamoto Y, De Silva R, Rhodes CG, et al. A new strategy for the assessment of viable myocardium and regional myocardial blood flow using ^{15}O-water and dynamic positron emission tomography. *Circulation.* 1992;86:167–178.
26. Watabe H, Jino H, Kawachi N, et al. Parametric imaging of myocardial blood flow with ^{15}O-water and PET using the basis function method. *J Nucl Med.* 2005;46:1219–1224.
27. Boellaard R, Knaapen P, Rijbroek A, Luurtsema GJ, Lammertsma AA. Evaluation of basis function and linear least squares methods for generating parametric blood flow images using ^{15}O-water and positron emission tomography. *Mol Imaging Biol.* 2005;7:273–285.
28. Iida H, Rhodes CG, De Silva R, et al. Myocardial tissue fraction–correction for partial volume effects and measure of tissue viability. *J Nucl Med.* 1991;32:2169–2175.
29. Harms HJ, de Haan S, Knaapen P, Allaart CP, Lammertsma AA, Lubberink M. Parametric images of myocardial viability using a single ^{15}O-H_2O PET/CT scan. *J Nucl Med.* 2011;52:745–749.
30. Rimoldi OE, Drake-Holland AJ, Noble MI, Camici PG. Basal and hyperaemic myocardial blood flow in regionally denervated canine hearts: an in vivo study with positron emission tomography. *Eur J Nucl Med Mol Imaging.* 2007;34:197–205.